JACS
JOURNAL OF THE AMERICAN CHEMICAL SOCIETY

Article

pubs.acs.org/JACS

Time-Dependent CO_2 Sorption Hysteresis in a One-Dimensional Microporous Octahedral Molecular Sieve

Laura Espinal,*[,†] Winnie Wong-Ng,[†] James A. Kaduk,[‡] Andrew J. Allen,[†] Chad R. Snyder,[†] Chun Chiu,[†,∥] Daniel W. Siderius,[†] Lan Li,[†] Eric Cockayne,[†] Anais E. Espinal,[§,⊥] and Steven L. Suib[§]

[†]Material Measurement Laboratory, National Institute of Standards and Technology, Gaithersburg, Maryland 20899, United States
[‡]BCS Chemistry Division, Illinois Institute of Technology, Chicago, Illinois 60616, United States
[§]Institute of Materials Science, University of Connecticut, Storrs, Connecticut 06269-3136, United States

Supporting Information

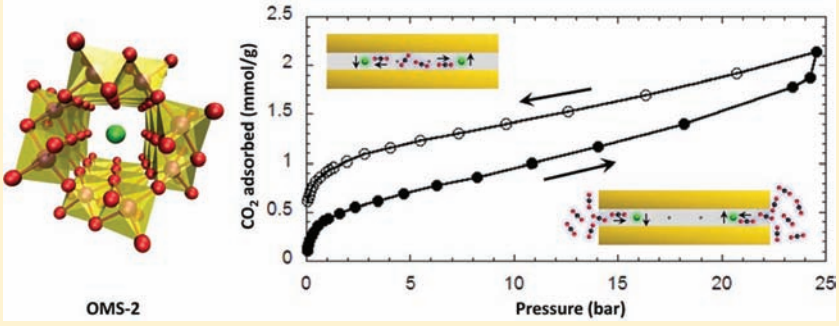

ABSTRACT: The development of sorbents for next-generation CO_2 mitigation technologies will require better understanding of CO_2/sorbent interactions. Among the sorbents under consideration are shape-selective microporous molecular sieves with hierarchical pore morphologies of reduced dimensionality. We have characterized the non-equilibrium CO_2 sorption of OMS-2, a well-known one-dimensional microporous octahedral molecular sieve with manganese oxide framework. Remarkably, we find that the degree of CO_2 sorption hysteresis increases when the gas/sorbent system is allowed to equilibrate for longer times at each pressure step. Density functional theory calculations indicate a "gate-keeping" role of the cation in the tunnel, only allowing CO_2 molecules to enter fully into the tunnel via a highly unstable transient state when CO_2 loadings exceed 0.75 mmol/g. The energy barrier associated with the gate-keeping effect suggests an adsorption mechanism in which kinetic trapping of CO_2 is responsible for the observed hysteretic behavior.

INTRODUCTION

Fundamental understanding of the interaction between CO_2 and the pore microstructures of solid sorbents and membranes is critical to advancing the design of cost-efficient porous carbon capture materials.[1] Conventional characterization of porous solids based on gas adsorption generates sorption isotherms with distinct shapes that reflect the interplay between the adsorbate/adsorbate and adsorbate/sorbent interactions, as well as effects of spatial confinement imposed by the porous host on any fluid phase transitions.[2] Sorption hysteresis occurs when the response of the adsorption system (adsorbate/sorbent) to gas loading differs from that of gas unloading due to a variety of factors. Depending on the adsorption system, hysteresis can be due to a pair of complementary capillary phase transitions,[3] sorbent structure transformations,[4] physical and chemical interactions between the adsorbate and sorbent,[5] and/or kinetic gas trapping.[6] Consequently, the shape of (hysteretic and non-hysteretic) gas sorption isotherms provides information about morphological features of the porous media and the physical and chemical interactions between adsorptive molecules and the pore constituents.

CO_2 sorption isotherms of candidate carbon capture materials are typically reported under equilibrium conditions. Although equilibrium isotherms provide important information about gas/solid interactions within the porous morphology, non-equilibrium isotherms provide information about intermediate states that may arise and disappear at different stages during the adsorption and desorption process. Knowledge of the atomic-scale rearrangements associated with such transient states is needed in order to determine how to increase sorbent lifetime in terms of multiple adsorption/desorption cycles, an important measure of performance for carbon capture materials. While great progress has been made in understanding the sorption dynamics in selected systems, such as cyclohexane sorption in porous glass,[7] H_2, Ar, and N_2 sorption in metal–organic frameworks,[8] and water sorption in microporous carbons,[9] close examination of experimental non-equilibrium CO_2 sorption in porous solids remains largely unexplored.

Received: March 1, 2012
Published: April 6, 2012

dx.doi.org/10.1021/ja3014133 | J. Am. Chem. Soc. 2012, 134, 7944–7951

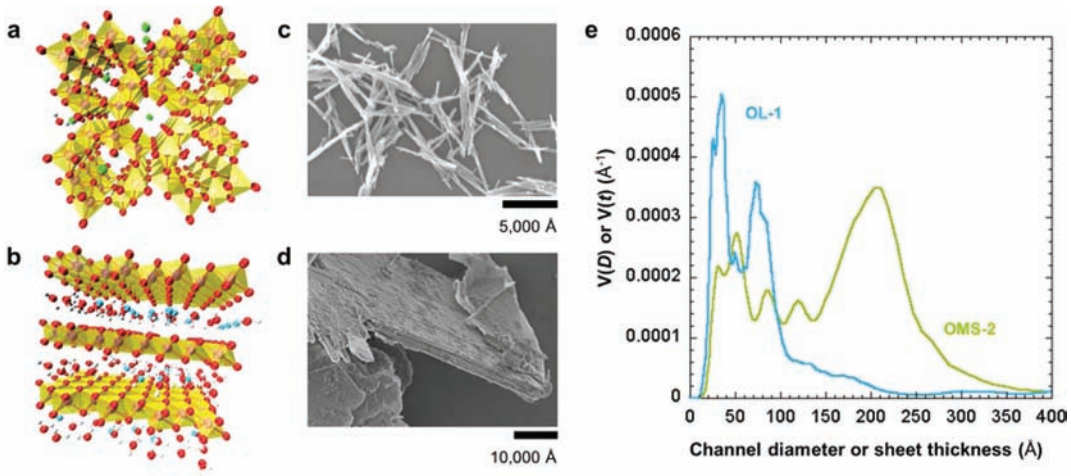

Figure 1. Crystal structure, particle morphology, and volume fraction size distribution for OMS-2 and OL-1. (a) A perspective drawing of the solid-state X-ray crystal structure of OMS-2, showing the octahedrally coodinated atoms covalently linked into a porous framework: red, O; purple, Mn; green, K; white, H. For clarity, translucent yellow walls are shown to highlight the location of the octahedrally coordinated Mn and show the tunnels as well as the cations and water molecules within the porous structure (van der Waals radii were not included). (b) A perspective drawing of the solid-state X-ray crystal structure of OL-1 showing the octahedrally coordinated atoms covalently linked into a porous framework: red, O; purple, Mn; blue, Na; white, H. For clarity, translucent yellow walls are shown to highlight the location of the octahedrally coordinated Mn and show the layer-shaped pores as well as the cations and water molecules within the porous structure (van der Waals radii were not included). (c) SEM image of OMS-2 particles showing the needle morphology. (d) SEM image of OL-1 particles showing the sheet-like morphology. (e) Volume fraction size distributions for OMS-2 with respect to tunnel or needle diameter (green) and for OL-1 with respect to sheet-like or layered pore thickness (light blue). A linear size scale is used, and only the fine primary features are included.

Crystalline microporous molecular sieves are of great interest for the gas separation industry,[10] in large part because of their adjustable structural and chemical parameters. In particular, the inherent affinity of CO_2 toward zeolites makes them ideal candidates for separating CO_2 from gas mixtures.[11] Additionally, the pore size tunability of titanium silicate octahedral/tetrahedral molecular sieves has proved valuable for controlling the adsorption uptake of gas molecules with comparable kinetic diameters.[12] In the present study, we explore the CO_2 and N_2 sorption properties of cryptomelane OMS-2, a molecular sieve composed of edge-sharing and mixed-valent manganese oxide octahedra units linked into a nanoporous framework.[13,14] The charge imbalance in the OMS-2 framework is balanced by K^+ and H_3O^+ (or H_2O) located in the one-dimensional tunnels, which have a pore diameter (4.60 Å)[15] comparable to the kinetic diameter of CO_2 (3.30 Å).[16] OMS-2 was selected as a model for this work based on its one-dimensional (1D) pore geometry, which offers guest molecules and cations within the 1D pores or tunnels limited degrees of freedom compared to a two-dimensional (2D) layered octahedral molecular sieve of similar pore aperture,[13,14] e.g., OL-1. Our experiments demonstrate that experimental temperature and gas loading affect the occurrence of CO_2 sorption hysteresis in OMS-2. Further, we show that the width of the hysteresis increases when the system is allowed to equilibrate for longer times (at intervals between 1 and 30 min), which contrasts with an intuitive expectation that a system moving toward equilibrium should exhibit reduced hysteresis. Based on these observations and density functional theory (DFT) calculations, we propose a possible CO_2 sorption mechanism involving transient rearrangements of the framework and other pore structure constituents.

EXPERIMENTAL AND COMPUTATIONAL SECTION

Sample Preparation. Cryptomelane OMS-2 was synthesized by a reflux method according to a procedure reported in the literature.[17] Briefly, 13.3 g of $KMnO_4$ in 225 mL of distilled deionized water (DDW) was added to a solution of 19.8 g of $MnSO_4{\cdot}H_2O$ in 67.5 mL of DDW and 6.8 mL of concentrated HNO_3. The resultant solution was kept under reflux at 373 K for 24 h with continuous stirring. The precipitated solids were filtered, washed with DDW, and dried overnight at a 393 K in air. Na-(Mg)-Birnessite OL-1 was synthesized according to a modified procedure reported in the literature.[18] In a typical experiment, 50 g of NaOH was dissolved in 200 mL of DDW while stirring with a magnetic bar. After the NaOH solution was cooled in an ice bath, 3.8 g of $KMnO_4$ (24.04 mmol) was added to the NaOH solution under stirring. The resultant solution was added slowly to a solution of 15.15 g of $Mn(Ac)_2{\cdot}4H_2O$ (61.82 mmol) and 2.265 g of $Mg(Ac)_2{\cdot}4H_2O$ (10.56 mmol) in 200 mL of DDW under vigorous agitation, keeping the temperature at 273 K, producing a brownish black suspension of MnO_x. The suspension was left under agitation at 273 K for 1 h before aging at 333 K for 48 h. The resultant solids were filtered, washed with DDW, and dried overnight at 333 K to get birnessite (OL-1).

Characterization. OMS-2 and OL-1 samples were characterized by X-ray diffraction (XRD), enegry-dispersive X-ray spectroscopy (EDX), and scanning electron microscopy (SEM). N_2 sorption experiments at 77 K were performed to calculate the surface area based on the multi-point Brunauer–Emmett–Teller (BET) method in the range from 0.05 to 0.30 relative pressure. High-resolution synchrotron X-ray powder diffraction data were collected at 100 K using beamline 11-BM at the Advanced Photon Source (APS), Argonne National Laboratory, using an average wavelength of 0.412210 Å. Ultra-small-angle X-ray scattering (USAXS)[19] measurements were carried out at sector 15-ID (ChemMatCARS) at the Advanced Photon Source (APS), Argonne National Laboratory, Argonne, IL. Small-angle neutron scattering (SANS)[20] measurements were carried out using the NIST/NSF NG3 30 m SANS instrument at the National Institute of Standards and Technology (NIST) Center for Neutron Research (NCNR). Additional experimental details, crystallographic data, USAXS/SANS data, a complete volume fraction size distribution based on SANS, methods for data analysis, and a description of the computational method for calculating the largest spherical guest molecule (LSGM) can be found in the Supporting Information.

Thermal Gravimetric Analysis (TGA) and TGA/MS Measurements. TGA was performed in a high-pressure thermal gravimetric

dx.doi.org/10.1021/ja3014133 | J. Am. Chem. Soc. 2012, 134, 7944–7951

Table 1. Physical and Chemical Characteristics of OMS-2 and OL-1

characteristics		OMS-2	OL-1
chemical formula[a]	from XRD	$K_{0.1}MnO_2 \cdot 0.08H_2O$	$Na_{0.3}MnO_2 \cdot 0.93H_2O$[b]
	from USAXS/SANS	$K_{0.1}MnO_2 \cdot 0.38H_2O$	$Na_{0.3}MnO_2 \cdot 0.64H_2O$[b]
BET surface area[c]		108 m^2/g	79 m^2/g
pore width[d]	with v-site, excl. vdW	5.68 ± 0.034 Å	5.77 ± 0.029 Å
	with v-site, incl. vdW	2.68 ± 0.034 Å	2.77 ± 0.029 Å
	with cation, excl. vdW	3.71 ± 0.029 Å	3.67 ± 0.030 Å
	with cation, incl. vdW	0.59 ± 0.030 Å	0.59 ± 0.035 Å
particle morphology		needle	platelet
average particle dimensions[e]			
from SEM	small diameter or thickness	200−1000 Å	4700−6800 Å
	large length or diameter	3000−7000 Å	14800−54500 Å
from USAXS	diameter or thickness	70, 207, 664 Å	35, 85, 1000 Å
	length	700, 2070, 6640 Å	350, 850, 10000 Å

[a]Elemental composition estimated from EDX data. [b]Small amounts of magnesium detected in OL-1 were excluded in order to solve the crystal structure. [c]Based on N_2 sorption data at 77 K. Standard deviation is 15% of each value. [d]Pore widths derived from LSGM calculations. [e]Standard deviation in average particle size from USAXS measurements is 5% of each value.

analyzer. The mass loss percent was recorded while the sample was being evacuated from ambient pressure down to less than 133 Pa (1 Torr) at 298 K, and then heated from room temperature to 423 K for 150 min at a heating rate of 5 K/min. The TGA/MS profiles were acquired with the TGA equipment attached to a mass spectrometer. The mass loss percent and ion current signal for water were monitored while the sample was under flowing helium at a flow rate of 200 mL/min, first at 298 K for 240 min and then heated to 423 K for 240 min.

Density Functional Theory Calculations. Structural calculations were performed using the Vienna *ab initio* Simulation Package[21] (VASP) code based on self-consistent DFT. We used projector-augmented wave pseudopotentials[22,23] in conjunction with a plane wave expansion of the wave functions with a 400 eV cutoff energy. The spin-dependent generalized gradient approximation (GGA) with PBEsol (Perdew−Burke−Ernzerhof revised for solids) parametrization[24] was used. To treat Mn magnetism, we used a GGA+U approach,[25] with an effective on-site Coulomb value (U) of 2.8 eV and exchange value (J) of 1.2 eV for Mn. A 2×2×2 Monkhorst−Pack grid was used to sample the Brillouin zone. OMS-2 has a (2×2) + (1×1) tunnel structure, built from double chains of edge-sharing MnO_6 octahedra.[26] The pure MnO_2 cryptomelane unit cell has equilibrium DFT lattice parameters (*a*, *b*, and *c*) of 9.701, 2.856, and 9.685 Å. The cryptomelane OMS-2 structure is only stabilized with respect to the *β*-MnO_2 phase in the presence of additional species. To treat the partial occupancy of the K^+ ions, etc., we first tripled the cell along the *b* axis, obtaining a $Mn_{24}O_{48}$ supercell. K^+ cations and CO_2 molecules were then situated in the large (2×2) tunnels. To search for the stable structure and optimum lattice parameters, atoms, cell shape, and volume were allowed to fully relax. Relaxations of atomic positions and lattice vectors were performed until residual forces were 0.01 eV/Å or less.

Volumetric CO_2 and N_2 Sorption Experiments. CO_2 and N_2 sorption measurements were carried out on computer-controlled custom-built volumetric sorption equipment previously described in detail,[27] with an estimated reproducibility within 0.5% and isotherm data error bar of less than 2% compared to other commercial instruments.[27] Sample degassing, prior to CO_2 or N_2 sorption experiment, was done at 423 K under vacuum for 20 h. An outgassing step of 1 min (without heating) was used between CO_2 adsorption/desorption cycles.

RESULTS AND DISCUSSION

A perspective drawing of the X-ray crystal structure illustrates the morphological differences between the tunnel-shaped pores in OMS-2 (Figure 1a) and layered pores in OL-1 (Figure 1b). The morphological differences between these materials extend to microscopic scales, as evidenced by SEM analyses. As shown in Figure 1c, OMS-2 particles are needle-like with diameters ranging from 200 to 1000 Å. OL-1 particles are platelet-shaped with thicknesses between 4700 and 6800 Å (Figure 1d). USAXS analyses further demonstrate the hierarchical pore/solid structures, where OMS-2 and OL-1 present distinct volume size fractions at intermediate mesopore scales (Figure 1e), approximately between pore and particle sizes. Detailed crystallographic data and volume fraction size distribution can be found in Figure S1, Table S1−S3, and Figure S2.

A summary of the physical and chemical characteristics of OMS-2 and OL-1 is presented in Table 1. The elemental compositions were estimated from EDX. The water content in the chemical formulas was determined from XRD and a technique based on the ratio of the USAXS-to-SANS intensities measured for the same samples. The larger water content in OMS-2 estimated from USAXS/SANS compared to XRD indicates the presence of disordered hydrated regions in the material, as the sensitivity of the USAXS/SANS technique to the presence of hydrogeneous compounds is independent of the degree of crystallinity. Discrepancies in the water content of OL-1 derived from both techniques are likely due to a heterogeneous H_2O molecule distribution throughout the pore structure. For more information on the USAXS/SANS results, see Figure S3 and Table S4.

Nitrogen adsorption experiments at 77 K were performed to determine the surface areas of outgassed samples based on the BET method (Table 1). The larger surface area observed for OMS-2 (108 m^2/g) compared to OL-1 (79 m^2/g) is mostly attributed to smaller particle sizes in OMS-2. TGA/MS was employed to verify that water removal was achieved during the outgassing step prior to N_2 and CO_2 sorption experiments. In addition, confirmation of water removal was necessary for creating a computational model of the material. TGA results

dx.doi.org/10.1021/ja3014133 | J. Am. Chem. Soc. 2012, 134, 7944−7951

(Figure S4a–d) demonstrate that heating samples to 423 K for >2 h under either flowing helium or vacuum produces the same mass percent change. Further, TGA/MS data (Figure S4b,d) confirm that the heating procedure under flowing helium completely removes water, which strongly suggests that the same occurs under vacuum. Therefore, the evacuated materials can be modeled as crystal structures containing cations and v-sites (vacant sites within the unit cell not occupied by H_2O molecules or cations).

Having determined the crystal structure of the two systems, a computational method was used to obtain a visualization of the maximum space accessible to guest molecules within the unit cell containing cations or v-sites. The method consists of determining the largest spherical guest molecule (LSGM) admissible within the 1D tunnel (OMS-2) or 2D planar (OL-1) micropores with cations or v-sites. Table 1 shows the pore width for OMS-2 and OL-1, which were calculated from LSGMs for unit cells with cations or v-sites both including and excluding allowance for van der Waals interactions (vdW radii). (For vdW radii values used and schematic illustrations of the LSGMs, see Table S5 and Figure S5.) As shown in Table 1, OMS-2 and OL-1 have comparable LSGMs for each scenario. Taking the values obtained for OMS-2 as an example, the unit cell containing v-sites can fit LSGMs of approximately 2.68 Å in diameter (including vdW radii), whereas the unit cell containing cations reduces the LSGM size by 78%. Therefore, the presence of the cation in the tunnel restricts the entrance of CO_2 and N_2 molecules, which have kinetic diameters of 3.30 and 3.64 Å,[16] respectively.

The determination of all the physical and chemical characteristics described above for OMS-2 and OL-1 allows CO_2 sorption to be modeled for either material. However, the lower dimensionality of the OMS-2 pore network provides an ideal setting for studying its mechanism of CO_2 sorption. Volumetric gas adsorption experiments were carried out to probe the affinity of CO_2 and N_2 toward OMS-2 and evaluate the molecular size sieving ability of OMS-2 at 303 K up to 25 bar (Figure 2). The larger CO_2 uptake over N_2 observed for OMS-2 could be partially attributed to molecular size sieving effects, given the smaller kinetic diameter of CO_2 compared to that of N_2.[16,28] Pore volume calculations based on N_2 physisorption at 77 K for OMS-2 and OL-1 have yielded lower values compared to similar calculations based on CO_2 physisorption at 273 K, likely due to the smaller kinetic diameter of CO_2.[29] However, the higher electronic affinity of CO_2 toward OMS-2 compared to N_2 cannot be ruled out as an explanation. The chemical affinity of CO_2 toward similar manganese oxides has been exploited to quantify strong basic sites via temperature-programmed desorption[30] and CO_2 chemisorption methods at sub-atmospheric pressures.[31,32] Furthermore, interactions between the sorbent surface and the adsorptive molecules are known to be enhanced in pores of molecular-size dimensions, as the interaction potentials from opposite walls overlap.[2,3f,33]

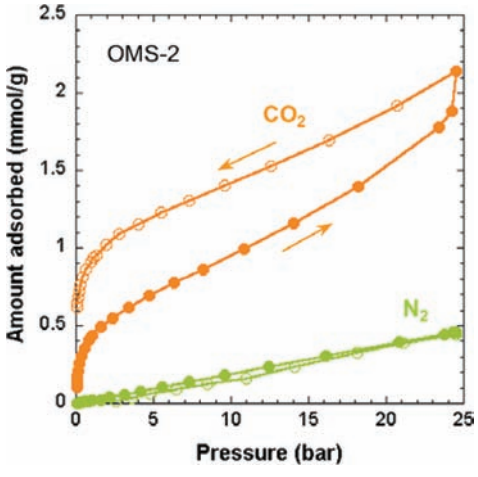

Figure 2. CO_2 and N_2 sorption uptake by OMS-2. Nitrogen (green) and carbon dioxide (orange) adsorption and desorption isotherms at T = 303 K using 15 min equilibration time for OMS-2. Solid and open symbols represent adsorption and desorption points, respectively.

Figure 2 shows that the CO_2 sorption isotherm for OMS-2 at 303 K up to 25 bar displays hysteretic behavior, which continues down to zero pressure on the desorption branch. Similar low-pressure hysteresis has been reported for CO_2 sorption on sodium alumino silicate-Type 4A zeolite at room temperature at pressures up to 20 bar.[11b] Such "open" hysteresis looping is typically associated with a volume change in the sorbent,[6a] irreversible uptake of gas molecules,[4c6a,] or chemisorption.[2] The presence of open hysteretic CO_2 sorption in OMS-2 strongly indicates that CO_2 molecules are able to enter the micropore space. However, a striking feature of the hysteresis was its time dependence, as revealed by volumetric CO_2 sorption experiments performed on OMS-2 using different equilibration times. (By "equilibration time" we refer to the time the material was exposed to the adsorptive gas at each pressure point, not the time to reach true thermodynamic equilibrium.) Figure 3a presents the CO_2 sorption isotherm for OMS-2 at 303 K for equilibration times of 1, 15, and 30 min. The width of the hysteresis loop increases as equilibration time is increased. For practical purposes, the material exhibiting increased hysteresis is referred to as "fresh" OMS-2, as this material was outgassed under heating at 423 K for at least 20 h to remove water prior to the series of CO_2 sorption experiments.

A contrasting behavior was observed for "aged" OMS-2, which was exposed to CO_2 at pressures above 20 bar for >20 h prior to the CO_2 sorption series. As shown in Figure 3b, the width of the hysteresis loops for aged OMS-2 decreases as equilibration time is increased, eventually leading to hysteresis closure for an equilibration time of 60 min. When aged OMS-2 is outgassed for more than 20 h, the behavior of fresh OMS-2 is recovered, where the hysteresis width increases with equilibration time. A possible kinetic CO_2 trapping occurs during aging of OMS-2, which explains the reduced extent of adsorption observed for aged OMS-2 compared to fresh OMS-2.

A fluid phase transition is not considered a potential driver for the hysteretic sorption because hysteresis closes after a sufficiently long equilibration time, and therefore the equilibrium sorption isotherm does not show coexisting phases. Moreover, the hysteresis continues down to zero pressure upon desorption, whereas a fluid phase transition would occur at a finite pressure and exhibit a discontinuous change in adsorbed density. Furthermore, in a condition of true equilibrium, phase coexistence and, hence, hysteresis for a fluid confined in a pore space is not possible above its "bulk fluid" critical temperature. As shown in Figure 3c, hysteresis still appears above the critical temperature of CO_2 (304.25 K), which rules out the possibility of a CO_2 phase transition causing the hysteresis.

CO_2 adsorption and desorption cycles were recorded up to different maximum pressures for OMS-2 at 303 K using 5 min

dx.doi.org/10.1021/ja3014133 | J. Am. Chem. Soc. 2012, 134, 7944–7951

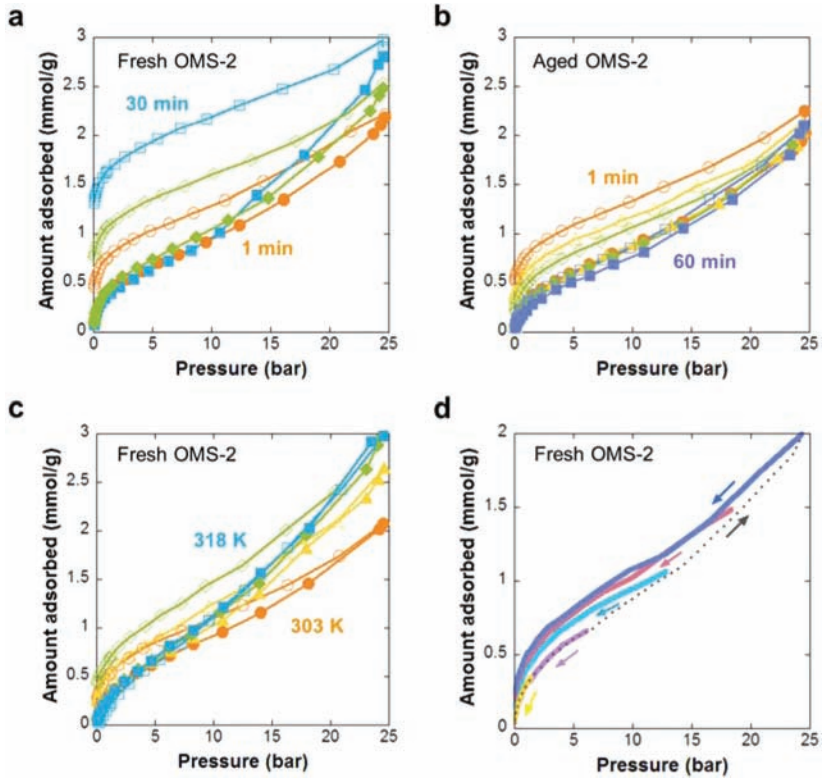

Figure 3. Effects of equilibration time, temperature, and pressure on CO_2 sorption hysteresis. Carbon dioxide adsorption (filled symbols) and desorption (open symbols) isotherms at T = 303 K at increasing equilibration times: 1 min (orange circles), 8 min (yellow triangles), 15 min (green diamonds), 30 min (light blue squares), and 60 min (dark blue squares) for (a) fresh OMS-2 and (b) aged OMS-2. Solid and open symbols represent adsorption and desorption points, respectively. (c) Carbon dioxide adsorption (filled symbols) and desorption (open symbols) isotherms for fresh OMS-2 using 15 min equilibration time at different temperatures: 303 K (orange circles), 308 K (yellow triangles), 313 K (green diamonds), and 318 K (light blue squares). (d) Scanning pressure curves using 5 min equilibration time for fresh OMS-2 at 303 K. The dotted line represents a common adsorption curve shared by all the scanning pressures curves. The colored solid lines represent desorption curves after reaching different maximum pressures on the adsorption branch. Hysteresis starts to appear at P > 7 bar.

of equilibration time, as shown in Figure 3d, where the dotted line indicates the common adsorption path followed in all runs. The onset of hysteresis occurs once the adsorption pressure exceeds 7 bar, or ~0.75 mmol of CO_2 adsorbed per gram of OMS-2. The presence of the 7 bar pressure threshold could indicate an onset of structural changes upon exposure to a larger concentration of CO_2 in the tunnels. However, *ex situ* XRD patterns (not shown here) of OMS-2 before and after exposure to 20 bar of CO_2 indicate no permanent structural change. Further *in situ* XRD experiments would be required to monitor changes in the OMS-2 crystal structure only present during exposure to CO_2 pressures >7 bar.

OMS-2 presents a distinct CO_2 sorption behavior that depends on equilibration time, temperature, maximum gas loading achieved, and material's history (i.e., fresh versus aged OMS-2). As hysteretic CO_2 sorption is itself evidence of CO_2 molecules penetrating into the micropores of OMS-2, we propose an atomic-scale mechanism of CO_2 sorption (Figure 4) supported with DFT calculations (Figure 5). Figure 4a provides a representative illustration of the front and cross-sectional side views of a single tunnel of OMS-2, highlighting the presence of cations and v-sites, which were created during the outgassing step (water removal) prior to CO_2 sorption experiments. The lack of hysteresis at CO_2 pressures below 7 bar can be explained if, during the adsorption step (Figure 4b), the CO_2 molecules diffuse into the OMS-2 tunnel until they encounter a cation, which behaves as a gate-keeper, restricting their further entrance into the tunnel, as expected from LSGM calculations. Upon desorption at this stage, the CO_2 molecules can easily exit the tunnel, with no hysteresis observed.

Above 7 bar, cations move slightly off the center-line of the tunnel (Figure 4c), which allows CO_2 molecules to move farther into the tunnel via the formation of a highly unstable intermediate state. The intermediate state is illustrated in Figure 4d, where a CO_2 molecule "sits" between the cation and the pore wall. The formation of a transient state not only allows for larger CO_2 uptakes but also exerts forces on the pore walls of OMS-2, which slightly deforms the crystal structure, as shown in Figure 4d. When the system is subjected to desorption at this stage, the CO_2 molecules already inside the tunnel must pass through the unstable state in reverse, which results in hysteretic behavior. The dissappearance of hysteresis at higher temperatures (Figure 3c) is a strong indicator of a reduced kinetic energy barrier for CO_2 adsorption above 7 bar due to an increased thermal vibration/mobility of cations and framework atoms, which allows CO_2 molecules to move farther into the tunnels. Finally, as shown in Figure 4e, kinetic trapping of CO_2 due to relaxation of stresses in OMS-2 (aging) occurs when the system is subjected to CO_2 pressures above 20 bar for >20 h, which results in reduced CO_2 uptake (Figure 3b).

DFT total energy calculations support the presence of a pressure threshold above which the energy cost of placing a CO_2 molecule on the side of the cation is significantly reduced. The formation energy of placing CO_2 in OMS-2 was computed

dx.doi.org/10.1021/ja3014133 | *J. Am. Chem. Soc.* 2012, 134, 7944−7951

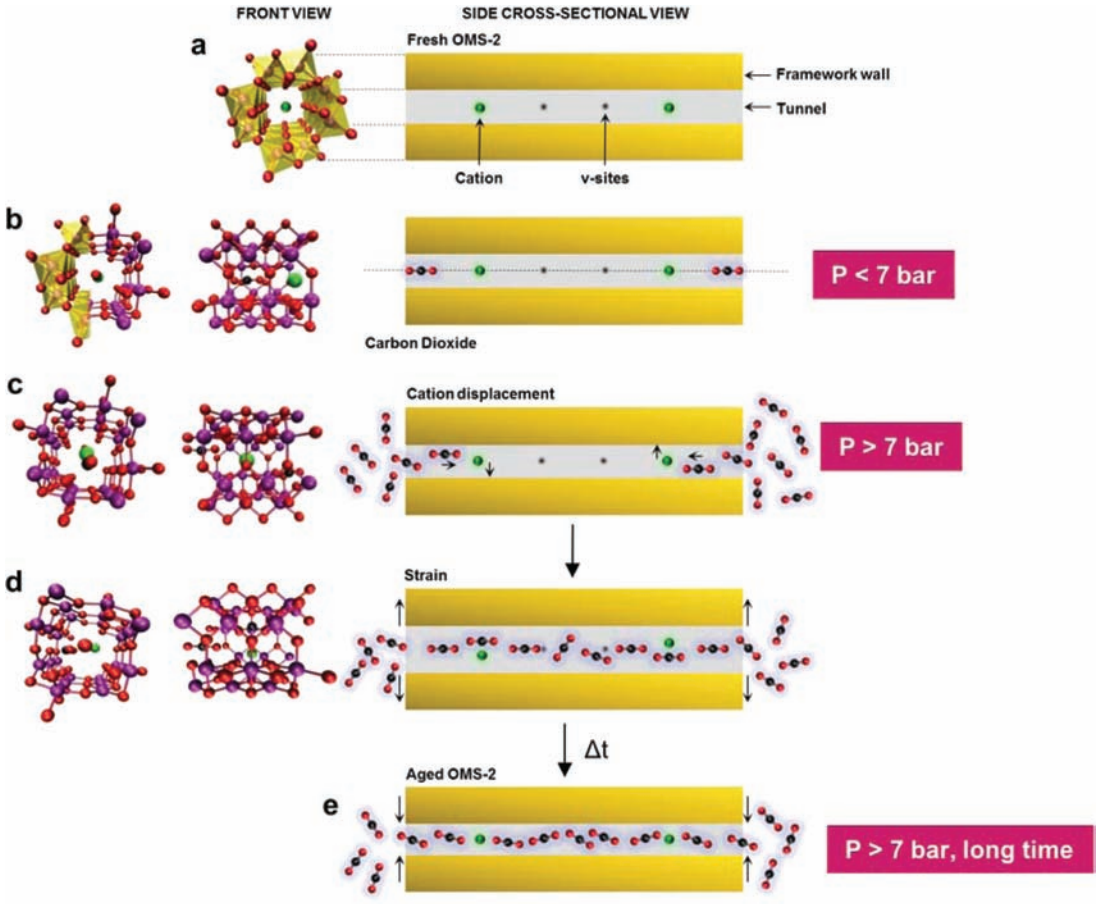

Figure 4. Possible CO_2 sorption mechanism by OMS-2 at 303 K. (a) Perspective view of a single tunnel of OMS-2 (front view) showing the cation inside the tunnel: red, O; purple, Mn; green K. For clarity, translucent yellow walls are shown to highlight the location of the octahedrally coordinated Mn (van der Waals radii were not included). (b–e) Schematic representation of the front and side views of the unit cell, and cross-sectional side view of the OMS-2 tunnel, showing a possible mechanism of CO_2 sorption as a function of pressure and time. The DFT equilibrium state of the system in (b) presents the following characteristics: the optimum distance between CO_2 and a potassium cation is 2.8 Å, the orientation of the CO_2 molecule is linearly aligned with the direction of the tunnel, and the center of the tunnel appears to be the more energetically favorable adsorption site for either CO_2 or cation. A soft glow surrounding the carbon dioxide molecules and cations represents a possible van der Waals exclusion volume.

using eq 1, where the first two terms refer to the total energies of OMS-2 with and without CO_2 adsorption, respectively; n specifies the number of CO_2 molecules; and E_{CO_2} is the energy of an individual CO_2 molecule.

$$E_f = \frac{(E_{\text{total,OMS-2 with CO}_2} - E_{\text{total,OMS-2 without CO}_2} - nE_{CO_2})}{n} \quad (1)$$

Because the onset of hysteresis occurs when adsorption pressures exceed 7 bar (equivalent to 0.75 mmol of CO_2/g OMS-2), DFT calculations were performed for OMS-2 containing zero, one, and two CO_2 molecules per unit cell, representing the systems under vacuum pressure, pressure <7 bar, and pressure >7 bar, respectively. The formation energies of the systems for the different scenarios are presented in Figure 5, where scenario a represents OMS-2 with no CO_2 (vacuum). For the system below 7 bar, two scenarios were considered. Scenario b represents the system where the CO_2 molecule is located in the "front" configuration (in front of the cation), and scenario c represents the system where the CO_2 molecule is located on the "side" configuration (on the side of the cation). The difference in the formation energies (ΔE_f) between scenarios b and c is ≈ 5.44 eV, implying a large energy cost to bypass the cation. Analogously, two scenarios were considered for the system above 7 bar. Scenario d represents the system where two CO_2 molecules are located in the front configuration, and scenario e represents the system where one CO_2 molecule is located in the front configuration and another one in the side configuration. The difference in the formation energies between scenarios d and e is given by $\Delta E_f \approx 0.13$ eV, which is significantly lower than that between scenarios b and c. Such results indicate that increasing the number of CO_2 molecules per unit cell from one to two leads to a more energetically stable "side" configuration, which symbolizes the weakening of the gate-keeping role of the cation and associated hysteretic sorption behavior. The DFT calculations strongly support experimental data, where the larger CO_2 uptakes observed for fresh OMS-2 above 7 bar are accompanied by an increased hysteresis width, whether these increased uptakes were achieved via longer equilibration times (Figure 3a) or larger adsorption pressures (Figure 3d).

■ CONCLUSIONS

The microporous octahedral molecular sieve we discuss here exhibits non-equilibrium hysteretic CO_2 sorption behavior

dx.doi.org/10.1021/ja3014133 | J. Am. Chem. Soc. 2012, 134, 7944–7951

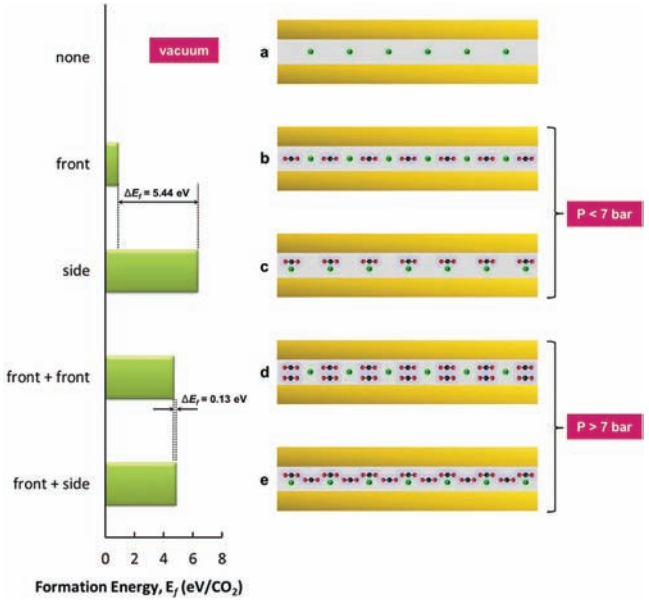

Figure 5. Formation energy of CO_2 in OMS-2. $E_f = (E_{total,OMS\text{-}2\ with\ CO_2} - E_{total,OMS\text{-}2\ without\ CO_2} - nE_{CO_2})/n$, where the first two terms refer to the total energies of OMS-2 with and without CO_2 adsorption, respectively; n specifies the number of CO_2 molecules; and E_{CO_2} is the energy of an individual CO_2 molecule. ΔE_f represents the difference between the formation energies of different OMS-2/CO_2 scenarios. OMS-2/CO_2 scenarios for which formation energies were calculated: (a) OMS-2 tunnel without CO_2, representing vacuum conditions; (b) OMS-2 tunnel at pressures below 7 bar, where one molecule of CO_2 is located in front of the cation within the unit cell; (c) OMS-2 tunnel at pressures below 7 bar, where one molecule of CO_2 is located on the side of the cation within the unit cell; (d) OMS-2 tunnel at pressures above 7 bar, where two molecules of CO_2 are located in front of the cation within the unit cell; (e) OMS-2 tunnel at pressures above 7 bar, where one molecule of CO_2 is located in front of the cation and another CO_2 molecule is located on the side, within the unit cell.

above 7 bar at temperatures below and above the bulk critical temperature of CO_2. Equilibration time, temperature, maximum CO_2 uptake achieved in the adsorption isotherm, and the history of the material significantly affect the occurrence of CO_2 sorption hysteresis in OMS-2. The observed hysteresis may be attributed to a combination of factors, including energetics of the formation of transient species, OMS-2 structural changes, and resultant constraints on diffusion. The CO_2 sorption properties of OMS-2 appear to be inherently linked to the degree to which the porous framework can resist internal forces derived from the presence of more than one CO_2 molecule per unit cell and then return to its original state upon release from the external stimuli for sufficient time. Further work is underway to verify experimentally the nature of the intermediate complexes, evaluate the effect of CO_2 exposure on the crystal structure of OMS-2 under *in situ* conditions, and monitor possible changes at larger characteristic length scales. Although this work considers a 1D (tunnel) pore system, we assert that our findings would be relevant to other promising CO_2 sorbent materials containing more complicated structures with "gated" pores. Furthermore, our results have implications for the development of next-generation time-resolved *in situ* characterization techniques for gas separation materials, as reliable data interpretation will depend critically on the extent to which the transient gas sorption properties of a material are known.

■ ASSOCIATED CONTENT

Supporting Information

Figure S1 and Tables S1−S3, detailed crystallographic data; Figure S2, complete volume fraction size distribution based on scattering data; Figure S3 and Table S4, additional USAXS/SANS results along with a full description of data analysis; Figures S4, TGA and TGA/MS data for samples being subjected to different drying conditions; description of the computational method for calculating LSGMs; Table S5, vdW radii values used for LSGM calculations; and Figure S5, a schematic illustration of the LSGMs for OMS-2 and OL-1. This material is available free of charge via the Internet at http://pubs.acs.org.

■ AUTHOR INFORMATION

Corresponding Author

laura.espinal@nist.gov

Present Addresses

[‖]Transportation Energy Technology, CanmetENERGY, Natural Resources Canada, Ottawa, ON K1A 1M1, Canada

[⊥]United Technologies Research Center, East Hartford, CT 06108

Notes

The authors declare no competing financial interest.

■ ACKNOWLEDGMENTS

L.E. thanks Alex Neimark for helpful discussions early in the early stages of this work. A.E.E. and S.L.S. acknowledge the support of the U.S. Department of Energy, Office of Basic Energy Sciences, Division of Chemical, Geochemical, and Biological Sciences. Dr. M. R. Suchomel at the Advanced Photon Source (Argonne National Laboratory) is acknowledged for assistance with the high resolution XRD data acquisition, Dr. J. Ilavsky (Argonne's X-ray Science Division) for assistance with the USAXS measurements, and Dr. S. R. Kline (NCNR) for assistance with the SANS measurements. The use of the Advanced Photon Source at Argonne National Laboratory was supported by the U.S. Department of Energy, Office of Science, Office of Basic Energy Sciences, under contract no. DE-AC02-06CH11357. ChemMatCARS, APS sector 15, is principally supported by the National Science Foundation/Department of Energy under grant no. CHE-0535644. This work also utilized neutron scattering facilities supported in part by the National Science Foundation under Agreement No. DMR-0454672.

■ REFERENCES

(1) Vaidhyanathan, R.; Iremonger, S. S.; Shimizu, G. K. H.; Boyd, P. G.; Alavi, S.; Woo, T. K. *Science* **2010**, *330*, 650−653.

(2) Lowell, S.; Shields, J. E.; Thomas, M. A.; Thommes, M. *Characterization of Porous Solids and Powders: Surface Area, Pore Size and Density*: Springer: Dordrecht, 2006.

(3) (a) Ball, P. C.; Evans, R. *Langmuir* **1989**, *5*, 714−723. (b) Wilkinson, N. J.; Duffy, J. A.; Fretwell, H. M.; Alam, M. A. *Phys. Lett. A* **1995**, *204*, 285−290. (c) Kierlik, E.; Monson, P. A.; Rosinberg, M. L.; Sarkisov, L.; Tarjus, G. *Phys. Rev. Lett.* **2001**, *87*, 055701. (d) Kleitz, F.; Berube, F.; Guillet-Nicolas, R.; Yang, C.-M.; Thommes, M. *J. Phys. Chem. C* **2010**, *114*, 9344−9355. (e) Burgess, C. G. V.; Everett, D. H.; Nuttall, S. *Pure Appl. Chem.* **1989**, *61*, 1845−1852. (f) Rouquerol, F.; Rouquerol, J.; Sing, K. *Adsorption by Powders and*

Porous Solids: Principles, Methodology and Applications; Academic Press: San Diego, CA, 1999. (g) Sing, K. S. W.; Everett, D. H.; Haul, R. A. W.; Moscou, L.; Pierotti, R. A.; Rouquerol, J.; Siemieniewska, T. *Pure Appl. Chem.* **1985**, *57*, 603−619. (h) Thommes, M. *Chem. Ing. Tech.* **2010**, *82*, 1059−1073.
(4) (a) Li, J.-R.; Kuppler, R. J.; Zhou, H.-C. *Chem. Soc. Rev.* **2009**, *38*, 1477−1504. (b) Braida, W. J.; Pignatello, J. J.; Lu, Y. F.; Ravikovitch, P. I.; Neimark, A. V.; Xing, B. S. *Environ. Sci. Technol.* **2003**, *37*, 409−417. (c) Zhao, X.; Xiao, B.; Fletcher, A. J.; Thomas, K. M.; Bradshaw, D.; Rosseinsky, M. J. *Science* **2004**, *306*, 1012−1015.
(5) (a) Southon, P. D.; Price, D. J.; Nielsen, P. K.; McKenzie, C. J.; Kepert, C. J. *J. Am. Chem. Soc.* **2011**, *133*, 10885−10891. (b) Bellat, J.-P.; Paulin, C.; Jeffroy, M.; Boutin, A.; Paillaud, J.-L.; Patarin, J.; Di Lella, A.; Fuchs, A. *J. Phys. Chem. C* **2009**, *113*, 8287−8295.
(6) (a) Bailey, A.; Cadenhead, D. A.; Davies, D. H.; Everett, D. H.; Miles, A. J. *Trans. Faraday Soc.* **1971**, *67*, 231−243. (b) Ravikovitch, P. I.; Neimark, A. V. *Adsorption—J. Int. Ads. Soc.* **2005**, *11*, 265−270.
(7) Valiullin, R.; Naumov, S.; Galvosas, P.; Kärger, J.; Woo, H.-J.; Porcheron, F.; Monson, P. A. *Nature* **2006**, *443*, 965−968.
(8) Sircar, S.; Wu, H.; Li, J.; Lueking, A. D. *Langmuir* **2011**, *27*, 14169−14179.
(9) Nakamura, M.; Ohba, T.; Branton, P.; Kanoh, H.; Kaneko, K. *Carbon* **2010**, *48*, 305−308.
(10) Kulprathipanja, S. *Zeolites in Industrial Separation and Catalysis*; Wiley-VCH: Weinheim, 2010.
(11) (a) Bonenfant, D.; Kharoune, M.; Niquette, P.; Mimeault, M.; Hausler, R. *Sci. Technol. Adv. Mater.* **2008**, *9*, 013007. (b) Siriwardane, R. V.; Shen, M.-S.; Fisher, E. P. *Energy Fuels* **2003**, *17*, 571−576.
(12) Kuznicki, S. M.; Bell, V. A.; Nair, S.; Hillhouse, H. W.; Jacubinas, R. M.; Braunbarth, C. M.; Toby, B. H.; Tsapatsis, M. *Nature* **2001**, *412*, 720−724.
(13) Suib, S. L. *J. Mater. Chem.* **2008**, *18*, 1623−1631.
(14) Suib, S. L. *Acc. Chem. Res.* **2008**, *41*, 479−487.
(15) Deguzman, R. N.; Shen, Y. F.; Neth, E. J.; Suib, S. L.; Oyoung, C. L.; Levine, S.; Newsam, J. M. *Chem. Mater.* **1994**, *6*, 815−821.
(16) Breck, D. *Zeolite Molecular Sieves: Structure, Chemistry, and Use*; Wiley: New York, 1974.
(17) Ghosh, R.; Shen, X. F.; Villegas, J. C.; Ding, Y. S.; Malinger, K.; Suib, S. L. *J. Phys. Chem. B* **2006**, *110*, 7592−7599.
(18) Luo, J.; Zhang, Q. H.; Huang, A. M.; Giraldo, O.; Suib, S. L. *Inorg. Chem.* **1999**, *38*, 6106−6113.
(19) Ilavsky, J.; Jemian, P. R.; Allen, A. J.; Zhang, F.; Levine, L. E.; Long, G. G. *J. Appl. Crystallogr.* **2009**, *42*, 469−479.
(20) Glinka, C. J.; Barker, J. G.; Hammouda, B.; Krueger, S.; Moyer, J. J.; Orts, W. J. *J. Appl. Crystallogr.* **1998**, *31*, 430−445.
(21) Kresse, G.; Furthmuller, J. *Phys. Rev. B* **1996**, *54*, 11169−11186.
(22) Blochl, P. E. *Phys. Rev. B* **1994**, *50*, 17953−17979.
(23) Kresse, G.; Joubert, D. *Phys. Rev. B* **1999**, *59*, 1758−1775.
(24) Perdew, J. P.; Ruzsinszky, A.; Csonka, G. I.; Vydrov, O. A.; Scuseria, G. E.; Constantin, L. A.; Zhou, X. L.; Burke, K. *Phys. Rev. Lett.* **2008**, *100*, 136406.
(25) Liechtenstein, A. I.; Anisimov, V. I.; Zaanen, J. *Phys. Rev. B* **1995**, *52*, R5467−R5470.
(26) Gao, T.; Glerup, M.; Krumeich, F.; Nesper, R.; Fjellvag, H.; Norby, P. *J. Phys. Chem. C* **2008**, *112*, 13134−13140.
(27) Zhou, W.; Wu, H.; Hartman, M. R.; Yildirim, T. *J. Phys. Chem. C* **2007**, *111*, 16131−16137.
(28) Cui, Y.; Kita, H.; Okamoto, K. *Chem. Commun.* **2003**, 2154−2155.
(29) Luo, J.; Zhang, Q. H.; Garcia-Martinez, J.; Suib, S. L. *J. Am. Chem. Soc.* **2008**, *130*, 3198−3207.
(30) Chen, X.; Shen, Y.-F.; Suib, S. L.; O'Young, C. L. *Chem. Mater.* **2002**, *14*, 940−948.
(31) Kumar, R.; Sithambaram, S.; Suib, S. L. *J. Catal.* **2009**, *262*, 304−313.
(32) Shen, X. F.; Ding, Y. S.; Liu, J.; Laubernds, K.; Zerger, R. P.; Polverejan, M.; Son, Y. C.; Aindow, M.; Suib, S. L. *Chem. Mater.* **2004**, *16*, 5327−5335.
(33) Yang, R. T. *Adsorbents: Fundamentals and Applications*; John Wiley & Sons, Inc.: Hoboken, NJ, 2003.